

Shape-Dependent Refractive Index Sensitivities of Gold Nanocrystals with the Same Plasmon Resonance Wavelength

Huanjun Chen, Lei Shao, Kat Choi Woo, Tian Ming, Hai-Qing Lin, and Jianfang Wang*

Department of Physics, The Chinese University of Hong Kong, Shatin, Hong Kong SAR, China

Received: August 1, 2009; Revised Manuscript Received: August 25, 2009

Gold nanocrystals in seven different shapes were prepared, including large nanorods, nanobipyramids, oxidized nanobipyramids, oxidized nanorods, dog-bone-like nanorods, peanut-like nanorods, and small nanorods. Their longitudinal plasmon resonance wavelengths were all synthetically controlled to be around 730 nm. Their refractive index sensitivities were measured by dispersing them in water–glycerol mixtures of varying compositions. The index sensitivities were found to be dependent on the shapes of the gold nanocrystals, with the large nanorods exhibiting the highest index sensitivity of 326 nm/RIU (refractive index unit) and the small nanorods exhibiting the lowest sensitivity of 156 nm/RIU. Finite-difference time-domain calculations were performed to obtain the electric field intensity enhancement contours around these gold nanocrystals. The index sensitivity was found to exhibit an approximately linear dependence on the product of the nanocrystal polarizability and end curvature.

1. Introduction

Noble metal nanocrystals exhibit rich plasmonic properties. Their localized surface plasmon resonances are highly dependent on the refractive index of the surrounding medium and generally shift toward the longer wavelengths as the index is increased.¹ This fascinating dependence makes noble metal nanocrystals ideal transducers that convert changes in the local refractive index into spectral shifts in the bright extinction and scattering spectra.^{2–4} Most organic and biological molecules possess higher refractive indices than aqueous buffer solutions. Their binding to the surfaces of metal nanocrystals causes the local refractive index to increase and thus the surface plasmon resonance peaks to red shift. The plasmon shifts indicate the presence of specific molecules. In addition, molecular binding and unbinding can also be monitored in real time with high sensitivity by measuring the plasmon shift continuously. Two methods are often employed to measure the plasmon shift.^{5–24} One is transmission spectrometry, which measures extinction, the sum of absorption, and scattering.^{5–10,12,14,15,17–24} This method is simple and inexpensive. It is suitable for ensemble metal nanocrystals dispersed in solutions or deposited on planar substrates. The other one is single-particle dark-field scattering, which measures scattering only.^{11,13,16} Single-particle measurements offer improved absolute detection limits and enable higher spatial resolution in multiplexed assays.

The index change-based sensing capability of noble metal nanocrystals has been unambiguously demonstrated in a number of studies. For example, lithographically fabricated Ag nanocrystal arrays have index sensitivities of ~ 200 nm/RIU.^{5–7} Their plasmon resonance peaks red shift by 3 nm per CH₂ unit when alkanethiol monolayers are formed on the metal surface.^{8–10} The use of single Ag triangular nanoprisms further improves the sensitivity to 4.4 nm per CH₂ unit for self-assembled alkanethiol monolayers.¹¹ Such high sensitivities of noble metal nanocrystals have allowed for the fabrication of optical biosensors for

detecting proteins,^{12–16} antigens,^{17–22} and the biomarker for Alzheimer's disease,^{23,24} and for monitoring their binding interactions.

The refractive index sensitivity of noble metal nanocrystals is a key factor in determining the detection sensitivity of metal nanocrystal-based biosensors and realizing their practical applications. Further improvement of the index sensitivities of metal nanocrystals requires the identification of pivotal structural and plasmonic parameters for index sensitivities. Such fundamental understanding can allow us to judiciously design metal nanocrystals with superior index sensitivities. A number of experimental and theoretical studies have been devoted to the measurement of refractive index sensitivities of metal nanocrystals both on the ensemble^{25–28} and single-particle levels.^{29–35} The shapes of metal nanocrystals that have been investigated include spheres, rods, cubes, plates, core–shell structures, and asymmetric particles. Most of these previous investigations have focused on metal nanocrystals with one particular shape in one study. Systematic studies, where the refractive index sensitivities of metal nanocrystals with different shapes, sizes, and plasmon resonance wavelengths are measured under well-controlled conditions and compared carefully, have remained limited.

We have recently measured the index sensitivities of Au nanospheres, nanocubes, nanobranches, nanorods, and nanobipyramids that exhibit different plasmon resonance wavelengths.³⁶ By combining our results together with previous ones, we find that the index sensitivity generally increases both as the plasmon resonance wavelength for a fixed nanocrystal shape becomes longer and as the curvature of metal nanocrystals gets larger. For example, the index sensitivities of Au nanorods with longitudinal plasmon wavelengths of 653, 728, and 846 nm are 195, 224, and 288 nm/RIU, respectively.³⁶ Au nanospheres of plasmon wavelengths at 530 nm exhibit the smallest index sensitivities around 40 nm/RIU,³⁶ while the index sensitivities of Au nanobranches of plasmon wavelengths at 1140 nm and nanocrescents of plasmon wavelengths at 2640 nm reach 700 and 880 nm/RIU, respectively.^{34,36} However, because the relationship between the plasmon resonance wavelength and the nanocrystal shape is very complex, it has remained difficult to

* To whom correspondence should be addressed. Phone: +852 3163 4167. Fax: +852 2603 5204. E-mail: jfwang@phy.cuhk.edu.hk.

differentiate between the effects of the plasmon resonance wavelength and the nanocrystal shape on the index sensitivity. The question of how the refractive index sensitivities of metal nanocrystals depend specifically on their shapes has remained unanswered. Here we report our studies on the refractive index sensitivities of Au nanocrystals that exhibit seven different shapes but have the same longitudinal plasmon wavelength at 730 nm. The Au nanocrystals are large nanorods (NRs), nanobipyramids (NBPs), oxidized NBPs, oxidized NRs, dog-bone-like NRs, peanut-like NRs, and small NRs. The measured index sensitivities range from 156 to 326 nm/RIU, with the large NRs exhibiting the highest index sensitivity and the small NRs exhibiting the lowest one. Finite-difference time-domain (FDTD) calculations have been carried out to investigate the effects of plasmon-related parameters on the refractive index sensitivities of metal nanocrystals.

2. Experimental Section

Growth of Gold Nanocrystals. Gold chloride trihydrate ($\text{HAuCl}_4 \cdot 3\text{H}_2\text{O}$), sodium borohydride (NaBH_4), silver nitrate (AgNO_3), cetyltrimethylammonium bromide (CTAB), sodium citrate dihydrate, ascorbic acid, hydrochloric acid (HCl), and glutathione were purchased from Sigma-Aldrich. Cetyltributylammonium bromide (CTBAB) was prepared according to a reported procedure.³⁷ Deionized water was used throughout all of the preparations.

Gold nanocrystals in seven different shapes were grown by using a seed-mediated method together with anisotropic oxidation and transverse overgrowth. Large NRs were prepared following a reported procedure.³⁸ Specifically, the seed solution was prepared by the addition of a freshly prepared, ice-cold aqueous NaBH_4 solution (0.01 M, 0.6 mL) into an aqueous mixture composed of HAuCl_4 (0.01 M, 0.25 mL) and CTAB (0.1 M, 9.75 mL), followed by rapid inversion mixing for 2 min. The resulting seed solution was kept at room temperature for 2 h before use. The growth solution was made by the sequential addition of aqueous HAuCl_4 (0.01 M, 2 mL), AgNO_3 (0.01 M, 0.6 mL), HCl (1.0 M, 0.8 mL), and ascorbic acid (0.1 M, 0.32 mL) solutions into an aqueous CTAB (0.1 M, 40 mL) solution. The resulting solution was mixed by swirling for 30 s. The CTAB-stabilized seed solution was diluted by 10 times with water and 100 μL of the diluted seed solution was added into the growth solution. The resulting solution was gently inversion-mixed for 2 min and then left undisturbed overnight. The longitudinal plasmon wavelength of the large NRs is 732 nm.

The above procedure was also employed to prepare Au NRs with a longitudinal plasmon wavelength of 955 nm by adding the original, undiluted seed solution (300 μL) in the growth solution. The obtained NRs were subjected to anisotropic oxidation³⁹ by adding HCl (1.0 M, 0.2 mL) in the as-prepared NR solution (10 mL), followed by bubbling O_2 into the mixture for 10 min. The plastic tube containing the mixture was kept uncapped and transferred in an isothermal oven at 65 °C to start oxidation. Extinction spectra of the NR solution were measured from time to time to monitor the oxidation process. When the desired longitudinal plasmon wavelength was obtained, the NRs were washed by two cycles of centrifugation (8000 $\times g$, 10 min) and redispersion in 0.1 M CTAB solutions to remove HCl. The resulting NRs are named oxidized NRs. They have a longitudinal plasmon wavelength at 733 nm.

For the preparation of small NRs, a previously reported seed-mediated procedure⁴⁰ was modified to first grow Au NRs with a longitudinal plasmon wavelength of 810 nm. Briefly, the seed solution was prepared by the addition of NaBH_4 (0.01 M, 0.3

mL) into an aqueous mixture composed of HAuCl_4 (0.01 M, 0.125 mL) and CTAB (0.1 M, 3.75 mL). The growth solution was made by the sequential addition of HAuCl_4 (0.01 M, 1.8 mL), AgNO_3 (0.01 M, 0.27 mL), and ascorbic acid (0.1 M, 0.288 mL) into CTAB (0.1 M, 42.75 mL). Then 250 μL of the seed solution was added. The obtained Au NRs were subjected to anisotropic oxidation to give small NRs with a longitudinal plasmon wavelength of 733 nm.

The preparation of dog-bone-like NRs was similar to that of the NRs with a longitudinal plasmon wavelength of 810 nm, except that the amount of the seed solution was changed from 250 to 150 μL .

Peanut-like NRs were prepared by transverse overgrowth⁴¹ on pregrown Au NRs. The pregrown NRs have a longitudinal plasmon wavelength of 855 nm. Their growth procedure was similar to that of the NRs with a longitudinal plasmon wavelength of 955 nm, except that the amount of the seed solution was changed from 300 to 200 μL . The stock solution for overgrowth was made by mixing together CTAB (0.1 M, 42.75 mL), HAuCl_4 (0.01 M, 1.8 mL), AgNO_3 (0.01 M, 0.27 mL), and ascorbic acid (0.1 M, 0.288 mL). Before overgrowth, a glutathione solution (0.01 M, 150 μL) was added into 15 mL of the pregrown NR solution. After the resulting mixture was kept at room temperature for 2 h, 25 mL of the stock solution was added to start overgrowth. Extinction spectra were taken consecutively to monitor the overgrowth process. When the desired longitudinal plasmon wavelength was reached, the produced NRs were washed by centrifugation and redispersed in 0.1 M CTAB solutions.

Two Au NBP samples with longitudinal plasmon wavelengths of 729 and 886 nm were grown according to a reported seed-mediated procedure, using citrate-stabilized Au nanoparticles as seeds.⁴² For the preparation of seeds, aqueous solutions of HAuCl_4 (0.01 M, 0.125 mL) and sodium citrate (0.01 M, 0.25 mL) were first added to water (9.625 mL), and then a freshly prepared, ice-cold solution of NaBH_4 (0.01 M, 0.15 mL) was added under vigorous stirring. The resulting citrate-stabilized seed solution was kept at room temperature for 2 h before use. The growth solution was made by the sequential addition of HAuCl_4 (0.01 M, 1.2 mL), ascorbic acid (0.1 M, 0.402 mL), and AgNO_3 (0.01 M, 0.06 mL) into CTBAB (0.01 M, 28.5 mL). Then 0.45 mL of the seed solution was added to the growth solution, followed by gentle inversion mixing for 10 s. The resulting solution was left undisturbed overnight in an isothermal oven at 65 °C. The obtained Au NBPs have a longitudinal plasmon wavelength of 729 nm. The growth of the NBPs with a longitudinal plasmon wavelength of 886 nm was carried out by changing the citrate-stabilized seed solution from 0.45 to 0.20 mL. Anisotropic oxidation was performed on this NBP sample to produce oxidized NBPs with a longitudinal plasmon wavelength of 729 nm.

Instrumentation. Extinction spectra were measured with a Hitachi U-3501 UV–visible/NIR spectrophotometer. Scanning electron microscopy (SEM) images were acquired on a FEI Quanta 400 FEG microscope. Transmission electron microscopy (TEM) images were acquired with a FEI CM 120 microscope at 120 kV. Nanocrystal sizes were measured on TEM images, with ~ 200 particles measured per sample. For TEM characterization, as-prepared Au nanocrystal solutions (1 mL for each) were centrifuged at 12 000 $\times g$ for 10 min. The precipitates were redispersed in water (1 mL for each), centrifuged again at 12 000 $\times g$ for 6 min, and finally redispersed in water (0.1 mL for each). The resulting nanocrystal dispersions (0.01 mL for each) were drop-cast carefully on a lacey-Formvar copper grid

stabilized with a thin layer of carbon and allowed to dry in air overnight before TEM imaging.

Refractive Index Sensitivity Measurement. Water–glycerol mixtures of varying volume ratios were used to change the refractive index of the surrounding medium of Au nanocrystals. The volume percentage of glycerol in the liquid mixture was varied from 0% to 90% at a step of 10%. As-prepared Au nanocrystals were first centrifuged at $12\,000 \times g$ for 6 min and then redispersed in the water–glycerol mixtures. Extinction spectra of the resulting dispersion solutions of Au nanocrystals were measured. The plasmon shift was plotted as a function of the refractive index, and the refractive index sensitivity was determined by linear fitting. The figure of merit was the index sensitivity divided by the full width at half-maximum of the extinction peak taken from aqueous dispersions of Au nanocrystals.

FDTD Calculations. FDTD calculations were performed with FDTD Solutions 6.0, which was developed by Lumerical Solutions, Inc. The dielectric function of gold was formulated with the Drude model with parameters chosen to match the experimental dielectric data as close as possible. In calculation, an electromagnetic pulse with its wavelength ranging from 600 to 900 nm was launched into a box containing the target Au nanocrystal to simulate a propagating plane wave interacting with the nanocrystal. The Au nanocrystal and its surrounding medium inside the box were divided into 0.5 nm meshes. The electric field of the pulse was set along the length axis of the nanocrystal. The surrounding medium was taken as water with a refractive index of 1.333. The sizes and shapes of the Au nanocrystals in calculation were set to be as close as possible to those measured from TEM images. Specifically, oxidized and small NRs were modeled as cylinders capped with two half spheres at both ends. Peanut-like NRs were modeled as a cylinder at the middle waist and two larger spheres at both ends. The larger spheres were cut to form four facets symmetrically relative to the length axis. Dog-bone-like NRs were also modeled as a cylinder at the middle waist and two larger spheres at both ends. The larger spheres were faceted only at the end. Large NRs were modeled as an octagonal prism at the middle waist and two octagonal pyramids at both ends. Oxidized and unoxidized NBPs were modeled as two pentagonal pyramids with five faceted surfaces in the middle region and their apexes were modeled as spherical caps with five cut facets.

3. Results and Discussion

Gold nanocrystals were prepared by using a seed-mediated growth method in the presence of cationic ammonium surfactants as stabilizing agents.^{38,40,42} The obtained nanocrystals are encapsulated with the surfactants and positively charged. Anisotropic oxidation with O_2 as an oxidizing agent³⁹ and transverse overgrowth⁴¹ were employed to precisely tune the longitudinal plasmon wavelengths of the nanocrystals. Oxidation of CTAB-stabilized Au nanocrystals with O_2 produces water-dissolvable $AuBr_2^-$ ions, which were removed by centrifugation in our experiments. Figure 1 shows the representative SEM and TEM images of the nanocrystals in seven different shapes, including large NRs, NBPs, oxidized NBPs, oxidized NRs, dog-bone-like NRs, peanut-like NRs, and small NRs. The oxidized (Figure 1e) and small NRs (Figure 1h) are cylindrical in the middle section and capped with two half spheres at both ends. The large NRs are faceted at the side, as revealed by SEM imaging (Figure 1a). The cross section of the large NRs in the middle section is believed to be octagonal, according to previous high-resolution TEM characterizations.³⁷ The NBPs (Figure 1c) and oxidized NBPs (Figure 1d) possess ten side surfaces per

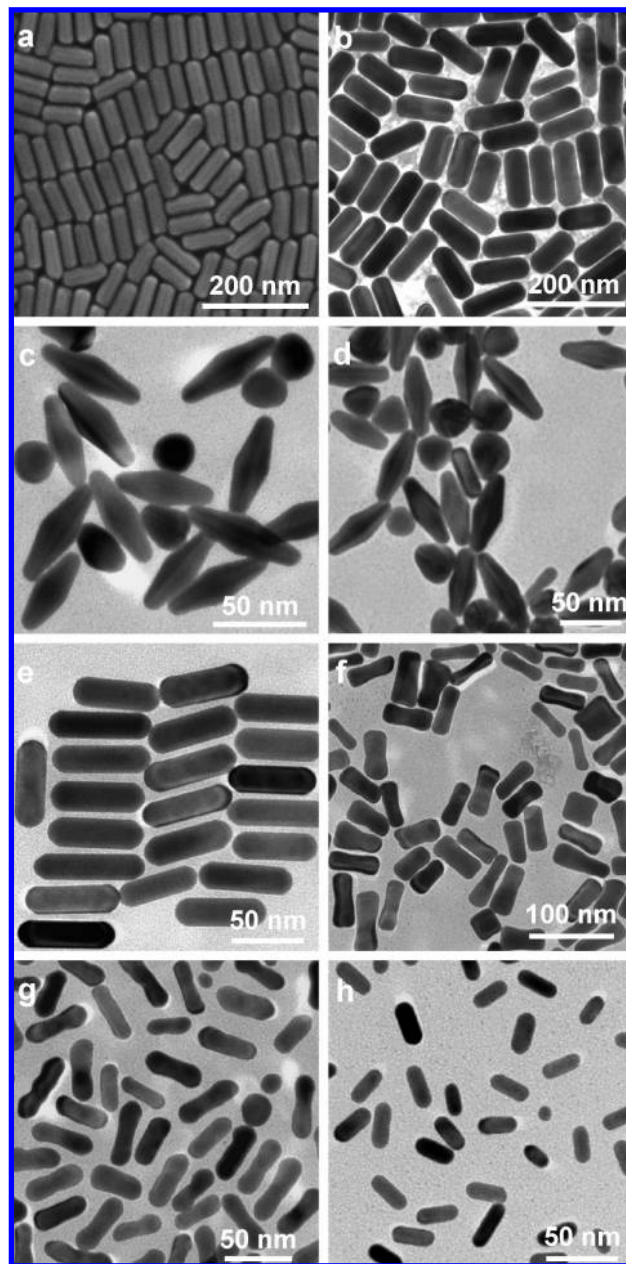


Figure 1. (a) SEM image of the large Au NRs. (b) TEM image of the large Au NRs. (c–h) TEM images of the NBPs, oxidized NBPs, oxidized NRs, dog-bone-like NRs, peanut-like NRs, and small NRs, respectively.

particle and their ends are rounded. The dog-bone-like NRs have two fatter ends and a thinner middle section (Figure 1f). The peanut-like NRs are similar to the dog-bone-like NRs in geometry, except that the fatter ends of the peanut-like NRs are more rounded (Figure 1g). The yields of the large, oxidized, small, dog-bone-like, and peanut-like NRs in terms of the particle number are $\sim 90\%$, and those of the oxidized and unoxidized NBPs are $\sim 60\%$. The sizes of these nanocrystals measured from their TEM images are listed in Table 1. The length was measured between the two farthest ends, and the diameter was measured at the middle waist. The sizes of these nanocrystals are relatively uniform. The percent errors, which are standard deviations divided by average values, are in the ranges of 4–10%, 6–15%, and 4–14% for the diameter, length, and aspect ratio, respectively. The particle volume ranges from 2 000 to 157 000 nm^3 and increases in the order of the small

TABLE 1: Sizes and Plasmon Resonance Wavelengths of the Gold Nanocrystals

Au nanocrystals	diameter ^a (nm)	length (nm)	aspect ratio	vol (nm ³)	curvature (10 ⁻³ nm ⁻¹)	LPRW ^b (nm)	fwhm ^c (nm)
large NRs	44 (2)	108 (7)	2.5 (0.2)	157 000	42 (4)	732	116
NBPs	19 (1)	55 (5)	2.9 (0.2)	11 000	200 (10)	729	91
oxidized NBPs	24 (1)	67 (4)	2.8 (0.1)	17 000	125 (5)	729	61
oxidized NRs	20 (1)	61 (5)	3.1 (0.3)	18 000	87 (3)	733	94
dog-bone-like NRs	20 (2)	56 (5)	2.8 (0.4)	21 000	100 (9)	732	125
peanut-like NRs	14 (1)	43 (4)	3.2 (0.4)	7 000	160 (15)	734	116
small NRs	10 (1)	26 (4)	2.6 (0.3)	2 000	122 (7)	733	98

^a The numbers in parentheses are standard deviations. The dimensions of the Au nanocrystals, including their diameter, length, aspect ratio, and curvature, were averaged over ~250 nanocrystals per sample. ^b LPRW represents the longitudinal plasmon resonance wavelength. ^c fwhm represents the full width at the half-maximum of the longitudinal plasmon resonance peak.

NRs, peanut-like NRs, NBPs, oxidized NBPs, oxidized NRs, dog-bone-like NRs, and large NRs. Because it is well-known that the maximum local electric field enhancement of metal nanocrystals depends strongly on the local curvature, the average local curvatures of the nanocrystals were also measured and included in Table 1. The curvature of each nanocrystal sample was measured at its sharpest points, which were assumed to be spherically truncated. Spherical crowns were first drawn on the TEM images of the Au nanocrystals to model the shapes and sizes of their sharpest points (Figure S1, Supporting Information). The base radius a and height h of each crown were then measured. The curvature was calculated according to $\sigma = 2h/(a^2 + h^2)$. The sharpest points of the dog-bone-like NRs are located at the circular edge at the end, while those of the other nanocrystals are located at both apexes.

Figure 2a shows the normalized extinction spectra of seven differently shaped Au nanocrystal samples that are dispersed in aqueous solutions. All of the nanocrystals exhibit two surface plasmon resonance peaks. The higher energy one is contributed by both the transverse plasmon resonance of the elongated Au nanocrystals and the plasmon resonance of the spherical Au nanocrystals that are present in the samples. The lower energy one arises from the longitudinal plasmon resonance of the elongated Au nanocrystals. In this study, we focus on the longitudinal surface plasmon resonance mode. Their longitudinal plasmon resonance wavelengths measured from the extinction peaks range from 729 to 734 nm and are very close to each other (Table 1). The full widths at the half maxima of the longitudinal extinction peaks are in the range of 60–125 nm, with the oxidized NBPs exhibiting the smallest peak width and the dog-bone-like NRs exhibiting the largest one. The difference in the peak width is mainly caused by the extent of the inhomogeneous size distribution, which varies among the Au nanocrystal samples because they were prepared under different conditions. The presence of the spherical Au nanocrystals does not interfere in the measurement of the refractive index sensitivities of the longitudinal plasmon resonances of the elongated Au nanocrystal samples because of the large separation between the higher and lower energy plasmon resonance peaks.

The Au nanocrystals were dispersed in water–glycerol mixtures to measure the refractive index sensitivities of their longitudinal plasmon resonance peaks. The refractive indices of the liquid mixtures were tuned by varying the volume percentage of glycerol (Table S1, Supporting Information). In our experiments, the highest volume percentage of glycerol that was used is 90%, because pure glycerol is too viscous. Panels b and c of Figure 2 show the extinction spectra of the large and small NR samples dispersed in the liquid mixtures of increasing volume percentage of glycerol as two representative examples. As the refractive index of the liquid mixture is increased, the

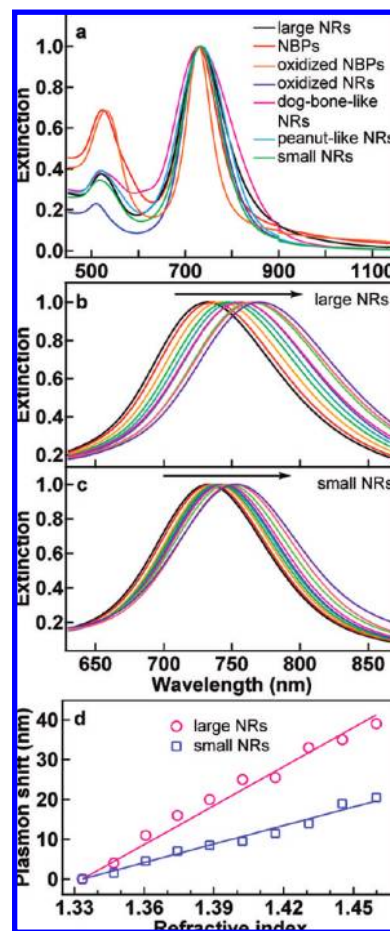


Figure 2. (a) Normalized extinction spectra of differently shaped Au nanocrystals dispersed in water. (b) Normalized extinction spectra of the large NRs dispersed in water–glycerol mixtures of varying compositions. (c) Normalized extinction spectra of the small NRs dispersed in water–glycerol mixtures of varying compositions. The arrows indicate the direction of increasing volume percentage of glycerol. (d) Dependence of the longitudinal plasmon shift on the refractive index of the liquid mixture for the large and small NR samples. The plasmon shift is relative to the longitudinal plasmon resonance wavelength measured when Au nanocrystals are dispersed in water. The lines are linear fits.

longitudinal plasmon resonance peaks of the nanocrystals shift toward longer wavelengths. The peak wavelengths in different liquid mixtures were measured and the longitudinal plasmon shifts were calculated by taking the difference relative to the longitudinal plasmon resonance wavelengths obtained in water. When the longitudinal plasmon shifts are plotted as a function of the refractive index of the liquid mixtures, an approximately linear dependence is observed (Figure 2d). Both plots can be

TABLE 2: Refractive Index Sensitivities, Figures of Merit, and Plasmonic Properties of the Gold Nanocrystals

Au nanocrystals	sensitivity (nm/RIU)	figure of merit	intensity enhancement ^a	decay length ^b (nm)	polarizability ^c (10 ⁶ nm)
large NRs	326	2.8	840	2.8	14.5
NBPs	301	3.3	5200	2.3	2.5
oxidized NBPs	264	4.3	3500	3.2	3.9
oxidized NRs	244	2.6	1600	4.3	5.3
dog-bone-like NRs	238	1.9	1900	3.6	3.0
peanut-like NRs	220	1.9	940	3.8	1.6
small NRs	156	1.6	1300	4.3	0.7

^a The maximum electric field intensity enhancement. ^b The length where the electric field intensity enhancement falls to $1/e$ of the maximum value along the direction perpendicular to the nanocrystal surface. ^c Polarizability $|\alpha| = (6\pi C_{\text{scat}})^{1/2}/k^2$, with C_{scat} being the scattering cross section obtained from FDTD calculations and k being the wavevector. Both C_{scat} and k values at the longitudinal plasmon resonance wavelength are used. The resulting polarizability therefore also refers to the value at this wavelength.

fitted well with lines. The slopes of the lines are the refractive index sensitivities. The index sensitivities of the large and small NR samples are determined in this way to be 326 and 156 nm/RIU, respectively. This procedure was also followed to determine the refractive index sensitivities of other Au nanocrystal samples (Figure S2, Supporting Information). The determined index sensitivities as well as the figures of merit are given in Table 2 for all of the nanocrystal samples.

Table 2 shows that the Au nanocrystals in different shapes exhibit different refractive index sensitivities even though their longitudinal plasmon wavelengths are all around 730 nm. The index sensitivities range from 156 to 326 nm/RIU and increase in the order of the small NRs, peanut-like NRs, dog-bone-like NRs, oxidized NRs, oxidized NBPs, NBPs, and large NRs. The highest index sensitivity is more than twice larger than the lowest one. These results suggest that the refractive index sensitivities of noble metal nanocrystals are highly dependent on their shapes and sizes even though their plasmon resonance wavelengths are the same. In a previous theoretical study, the index sensitivity has been found to be dependent solely on the plasmon resonance wavelength and independent of the shape and size for single-component noble metal nanocrystals.⁴³ In that study, metal nanocrystals in the shapes of highly regular cylinders, disks, and spherical shells are considered. They have either circular or spherical symmetries. The plasmon resonance condition is determined by the depolarization parameter, the real dielectric function of the metal, and the refractive index of the surrounding medium. This resonance condition leads to the exclusive dependence of the index sensitivity on the refractive index of the medium and the real dielectric function of the metal. In our studies, the Au nanocrystals are truncated and have more complex geometries. Their longitudinal plasmon resonance wavelengths are dependent not only on the aspect ratio, but also on the specific shape (Table 1). The resonance condition of these nanocrystals is much more complicated and cannot be described with a simple relationship. It is therefore very important to investigate and identify the determining factors for the refractive index sensitivity of noble metal nanocrystals that have different shapes but the same plasmon resonance wavelengths.

The refractive index sensitivities of noble metal nanocrystals are fundamentally determined by how easily the free electron cloud in metal nanocrystals is displaced relative to the positive atomic lattice by light.^{44,45} In physical terms, an increase in the medium dielectric constant, which is equal to the square of the refractive index for media with little absorption at the plasmon resonance wavelength, leads to more screening of the Coulombic restoring force acting on the free electrons in metal nanocrystals. The reduced restoring force thus results in a decrease in the plasmon resonance energy, which corresponds to a red shift in the plasmon resonance peak. The easier it is to displace the free electron cloud in metal nanocrystals, the more severe the

index increase-caused screening of the Coulombic restoring force becomes. The displacement pattern of the free electron cloud in metal nanocrystals depends not only on the net polarizability but also on the specific shape. Metal nanocrystals of complex shapes usually exhibit much higher charge densities in the surface regions with sharp curvatures. Because there are no analytic solutions for the polarizabilities of metal nanocrystals with complex shapes, we performed FDTD calculations to obtain the polarizabilities of the Au nanocrystals and investigated the effects of different factors on the refractive index sensitivity by taking into account the geometrical shape as well.

Figure 3 shows the electric field intensity enhancement contours and the extinction spectra obtained from FDTD calculations on the Au nanocrystals with seven different shapes. To better illustrate the shapes of the nanocrystals, the TEM images with each image containing a single nanocrystal are also provided. During FDTD calculation, the electric field is set to be polarized along the length axis. Therefore only the longitudinal plasmon resonance of the nanocrystals is calculated. The shape and size of each nanocrystal sample are adjusted to be as close as possible to the average experimental ones (Table 1), and the longitudinal plasmon wavelength is kept around 730 nm. The electric field intensity enhancement is nonuniform around each nanocrystal. The enhancement at the end surfaces is generally much larger than that at the side surfaces. For the dog-bone-like NR, the maximum enhancement is along the circular edge at the end, while for all of the other nanocrystals, the maximum enhancement is at the apex. The intensity enhancement decays rapidly away from the metal surface. From the field intensity enhancement contours, the maximum field intensity enhancement and the corresponding decay length of the enhancement are obtained and listed in Table 2. In addition, FDTD calculations also give the scattering cross sections of the metal nanocrystals at their longitudinal plasmon resonance wavelengths. From the scattering cross sections, the polarizabilities are obtained and also included in Table 2.

We plot the refractive index sensitivity as functions of different parameters of the Au nanocrystals in order to find out their effects on the index sensitivity. We first look at the geometrical parameters of the metal nanocrystals, including the particle volume and the local curvature, because in general, larger particle volumes lead to higher scattering cross sections and sharper local curvatures give larger local electric field enhancement. From the plots of the index sensitivity versus the particle volume (Figure 4a), no clear relationship is found. As the particle volume is increased from 2 000 to 20 000 nm³, the index sensitivity varies between 150 and 300 nm/RIU without showing a positive correlation. The particle volume of the large NRs is 14 times that of the NBPs, but the index sensitivity increases only from 301 to 326 nm/RIU. The particle volume of the NBPs is smaller than that of the dog-bone-like NRs, but

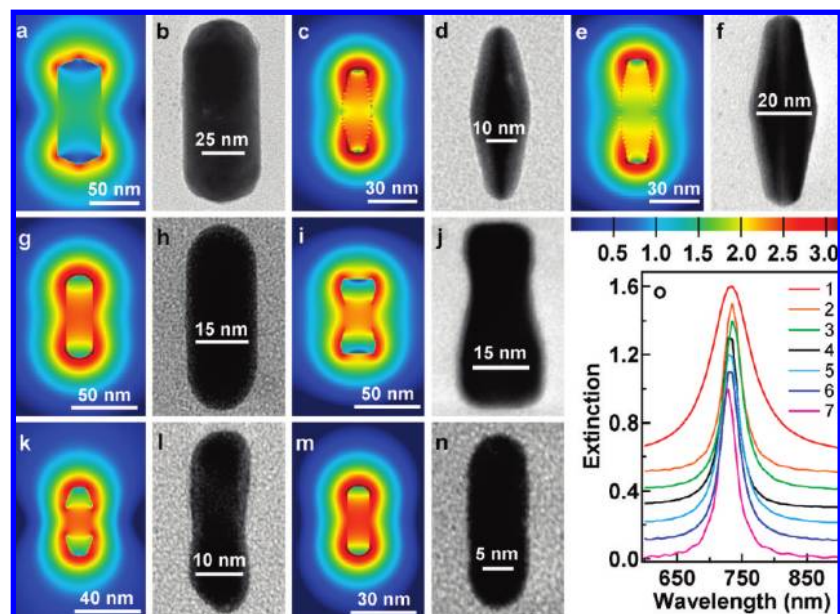


Figure 3. Electric field intensity enhancement contours (colored) and TEM images (gray) of differently shaped Au nanocrystals: (a, b) Large NRs; (c, d) NBPs; (e, f) oxidized NBPs; (g, h) oxidized NRs; (i, j) dog-bone-like NRs; (k, l) peanut-like NRs; and (m, n) small NRs. (o) Calculated extinction spectra of Au nanocrystals embedded in water. Curves 1 to 7 represent the large NRs, NBPs, oxidized NBPs, oxidized NRs, dog-bone-like NRs, peanut-like NRs, and small NRs, respectively. The field intensity enhancement is at the logarithmic scale.

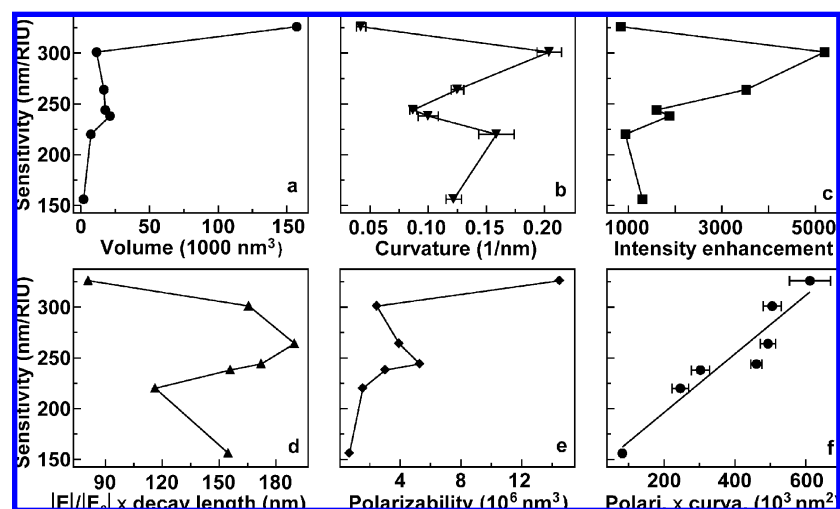


Figure 4. Relationship between the refractive index sensitivity and different parameters of the Au nanocrystals: (a) nanocrystal volume; (b) end curvature; (c) maximum electric field intensity enhancement; (d) product of the maximum field enhancement and the decay length of the field intensity enhancement along the central length axis of the Au nanocrystals; (e) polarizability; and (f) product of the polarizability and the end curvature.

the index sensitivity of the NBPs is larger than that of the dog-bone-like NRs. There is no positive correlation between the index sensitivity and the local curvature either (Figure 4b). The effects of parameters beyond the simple geometrical consideration on the index sensitivity need therefore to be further taken into account.

We next look at the plasmon resonance-related properties, including the maximum electric field intensity enhancement, the product of the maximum field enhancement and the decay length, and the polarizability. Figure 4c shows the plot of the index sensitivity versus the maximum electric field intensity enhancement. It is postulated that larger electric field enhancements lead to higher polarization of the molecules in the surrounding medium. The polarized medium can partially neutralize the charge density at the metal surface and thus reduce the plasmon resonance energy. However, no positive correlation is observed between the index sensitivity and the maximum

electric field intensity enhancement. In particular, the large NRs possess the largest sensitivity but their field intensity enhancement is the smallest. The electric field intensity enhancement is usually the largest in the region adjacent to the metal surface. It decays rapidly away from the metal surface. Previous experiments on index change-based sensing have shown that the region within the range of 10–20 nm on the metal surface is the most sensitive.^{10,14} We therefore consider the product between the maximum field enhancement and the decay length. Figure 4d shows the plot of the index sensitivity versus this product. Again, no positive correlation is found.

As mentioned above, the polarizability of metal nanocrystals plays an important role in the refractive index sensitivity. The index sensitivity is therefore plotted as a function of the polarizability, as shown in Figure 4e. There is no simple correlation between the index sensitivity and the polarizability, suggesting that there are also other factors taking effect on the

index sensitivity. We therefore plot the index sensitivity as a function of the product between the nanocrystal polarizability and the local curvature (Figure 4f). An approximate linear relationship is obtained. The index sensitivity increases as the polarizability-curvature product is increased, which is consistent with the above argument that both the polarizability and shape of metal nanocrystals play important roles on the index sensitivity.

4. Conclusions

In summary, we have prepared Au nanocrystals that exhibit seven different shapes but have the same longitudinal plasmon resonance wavelength at 730 nm. The refractive index sensitivities of these Au nanocrystals have been measured. They are in the range of 156 and 326 nm/RIU and increase in the order of small nanorods, peanut-like nanorods, dog-bone-like nanorods, oxidized nanorods, oxidized nanobipyramids, nanobipyramids, and large nanorods. Finite-difference time-domain calculations have been performed on these Au nanocrystals to obtain plasmon resonance-related properties. The index sensitivities have been plotted as functions of the plasmon resonance-related properties as well as the geometrical parameters of the nanocrystals. A linear relationship is found between the index sensitivity and the product between the polarizability and the curvature. These results are important not only for understanding the fundamental aspects of the refractive index sensitivity of noble metal nanocrystals but also for designing and developing ultrasensitive noble metal nanocrystal-based sensing devices.

Acknowledgment.

This work was supported by CUHK Research Excellence Award 2008–2009 (Project Code 4411435), RGC Research Grant Direct Allocation (Project Code 2060358), and National Natural Science Foundation of China (Project Code 20828001).

Supporting Information Available: Spherical crowns drawn on the TEM images of the Au nanocrystals, extinction spectra of other Au nanocrystals dispersed in water–glycerol mixtures of varying compositions, dependence of the plasmon shift on the refractive index of the liquid mixture for other Au nanocrystals, and refractive indices of water–glycerol mixtures of varying compositions. This material is available free of charge via the Internet at <http://pubs.acs.org>.

References and Notes

- Link, S.; El-Sayed, M. A. *J. Phys. Chem. B* **1999**, *103*, 8410.
- Willets, K. A.; Van Duyne, R. P. *Annu. Rev. Phys. Chem.* **2007**, *58*, 267.
- Murphy, C. J.; Gole, A. M.; Hunyadi, S. E.; Stone, J. W.; Sisco, P. N.; Alkilany, A.; Kinard, B. E.; Hankins, P. *Chem. Commun.* **2008**, 544.
- Anker, J. N.; Hall, W. P.; Lyandres, O.; Shan, N. C.; Zhao, J.; Van Duyne, R. P. *Nat. Mater.* **2008**, *7*, 442.
- Jensen, T. R.; Duval, M. L.; Kelly, K. L.; Lazarides, A. A.; Schatz, G. C.; Van Duyne, R. P. *J. Phys. Chem. B* **1999**, *103*, 9846.
- Malinsky, M. D.; Kelly, K. L.; Schatz, G. C.; Van Duyne, R. P. *J. Phys. Chem. B* **2001**, *105*, 2343.
- Haes, A. J.; Zou, S. L.; Schatz, G. C.; Van Duyne, R. P. *J. Phys. Chem. B* **2004**, *108*, 109.
- Malinsky, M. D.; Kelly, K. L.; Schatz, G. C.; Van Duyne, R. P. *J. Am. Chem. Soc.* **2001**, *123*, 1471.
- Haes, A. J.; Zou, S. L.; Schatz, G. C.; Van Duyne, R. P. *J. Phys. Chem. B* **2004**, *108*, 6961.
- Whitney, A. V.; Elam, J. W.; Zou, S. L.; Zinovev, A. V.; Stair, P. C.; Schatz, G. C.; Van Duyne, R. P. *J. Phys. Chem. B* **2005**, *109*, 20522.
- Sherry, L. J.; Jin, R. C.; Mirkin, C. A.; Schatz, G. C.; Van Duyne, R. P. *Nano Lett.* **2006**, *6*, 2060.
- Haes, A. J.; Van Duyne, R. P. *J. Am. Chem. Soc.* **2002**, *124*, 10596.
- Raschke, G.; Kowarik, S.; Franzl, T.; Sönnichsen, C.; Klar, T. A.; Feldmann, J.; Nichtl, A.; Kürzinger, K. *Nano Lett.* **2003**, *3*, 935.
- Marinakos, S. M.; Chen, S. H.; Chilkoti, A. *Anal. Chem.* **2007**, *79*, 5278.
- Chen, C.-D.; Cheng, S.-F.; Chau, L.-K.; Wang, C. R. C. *Biosens. Bioelectron.* **2007**, *22*, 926.
- Nusz, G. J.; Marinakos, S. M.; Curry, A. C.; Dahlin, A.; Höök, F.; Wax, A.; Chilkoti, A. *Anal. Chem.* **2008**, *80*, 984.
- Ribon, J. C.; Haes, A. J.; McFarland, A. D.; Yonzon, C. R.; Van Duyne, R. P. *J. Phys. Chem. B* **2003**, *107*, 1772.
- Wang, C. G.; Ma, Z. F.; Wang, T. T.; Su, Z. M. *Adv. Funct. Mater.* **2006**, *16*, 1673.
- Yu, C. X.; Irudayaraj, J. *Anal. Chem.* **2007**, *79*, 572.
- Gish, D. A.; Nsiah, F.; McDermott, M. T.; Brett, M. J. *Anal. Chem.* **2007**, *79*, 4228.
- Yu, C. X.; Irudayaraj, J. *Biophys. J.* **2007**, *93*, 3684.
- Mayer, K. M.; Lee, S.; Liao, H. W.; Rostro, B. C.; Fuentes, A.; Scully, P. T.; Nehl, C. L.; Hafner, J. H. *ACS Nano* **2008**, *2*, 687.
- Haes, A. J.; Hall, W. P.; Chang, L.; Klein, W. L.; Van Duyne, R. P. *Nano Lett.* **2004**, *4*, 1029.
- Haes, A. J.; Chang, L.; Klein, W. L.; Van Duyne, R. P. *J. Am. Chem. Soc.* **2005**, *127*, 2264.
- Yang, J.; Wu, J.-C.; Wu, Y.-C.; Wang, J.-K.; Chen, C.-C. *Chem. Phys. Lett.* **2005**, *416*, 215.
- Khlebtsov, N. G.; Trachuk, L. A.; Mel'nikov, A. G. *Opt. Spectrosc.* **2005**, *98*, 77.
- Khlebtsov, B. N.; Khlebtsov, N. G. *J. Quant. Spectrosc. Radiat. Transfer* **2007**, *106*, 154.
- Wu, C. L.; Xu, Q.-H. *Langmuir* **2009**, *25*, 9441.
- Mock, J. J.; Smith, D. R.; Schultz, S. *Nano Lett.* **2003**, *3*, 485.
- McFarland, A. D.; Van Duyne, R. P. *Nano Lett.* **2003**, *3*, 1057.
- Raschke, G.; Brogl, S.; Sucha, A. S.; Rogach, A. L.; Klar, T. A.; Feldmann, J.; Fieries, B.; Petkov, N.; Bein, T.; Nichtl, A.; Kürzinger, K. *Nano Lett.* **2004**, *4*, 1853.
- Sherry, L. J.; Chang, S.-H.; Schatz, G. C.; Van Duyne, R. P.; Wiley, B. J.; Xia, Y. N. *Nano Lett.* **2005**, *5*, 2034.
- Lee, K.-S.; El-Sayed, M. A. *J. Phys. Chem. B* **2006**, *110*, 19220.
- Bukasov, R.; Shumaker-Parry, J. S. *Nano Lett.* **2007**, *7*, 1113.
- Ni, W. H.; Chen, H. J.; Kou, X. S.; Yeung, M. H.; Wang, J. F. *J. Phys. Chem. C* **2008**, *112*, 8105.
- Chen, H. J.; Kou, X. S.; Yang, Z.; Ni, W. H.; Wang, J. F. *Langmuir* **2008**, *24*, 5233.
- Kou, X. S.; Zhang, S. Z.; Tsung, C.-K.; Yang, Z.; Yeung, M. H.; Stucky, G. D.; Sun, L. D.; Wang, J. F.; Yan, C. H. *Chem.—Eur. J.* **2007**, *13*, 2929.
- Ni, W. H.; Kou, X. S.; Yang, Z.; Wang, J. F. *ACS Nano* **2008**, *2*, 677.
- Tsung, C.-K.; Kou, X. S.; Shi, Q. H.; Zhang, J. P.; Yeung, M. H.; Wang, J. F.; Stucky, G. D. *J. Am. Chem. Soc.* **2006**, *128*, 5352.
- Sau, T. K.; Murphy, C. J. *Langmuir* **2004**, *20*, 6414.
- Kou, X. S.; Zhang, S. Z.; Yang, Z.; Tsung, C.-K.; Stucky, G. D.; Sun, L. D.; Wang, J. F.; Yan, C. H. *J. Am. Chem. Soc.* **2007**, *129*, 6402.
- Kou, X. S.; Ni, W. H.; Tsung, C.-K.; Chan, K.; Lin, H.-Q.; Stucky, G. D.; Wang, J. F. *Small* **2007**, *3*, 2103.
- Miller, M. M.; Lazarides, A. A. *J. Phys. Chem. B* **2005**, *109*, 21556.
- Jain, P. K.; El-Sayed, M. A. *J. Phys. Chem. C* **2007**, *111*, 17451.
- Jain, P. K.; El-Sayed, M. A. *Nano Lett.* **2008**, *8*, 4347.